

X-rays observations of a super-Chandrasekhar object reveal an ONeMg and a CO white dwarf merger product embedded in a putative SN Iax remnant [★]

Lidia M. Oskino^{1,2}, Vasilii V. Gvaramadze^{3,4,5}, Götz Gräfen⁶, Norbert Langer^{6,7}, Helge Todt¹

¹Institute of Physics and Astronomy, University of Potsdam, 14476 Potsdam, Germany
e-mail: lida@astro.physik.uni-potsdam.de

²Department of Astronomy, Kazan Federal University, Kremlevskaya Str 18, Kazan, Russia

³Sternberg Astronomical Institute, Lomonosov Moscow State University, Moscow, Russia

⁴Space Research Institute, Russian Academy of Sciences, Moscow, Russia

⁵Evgeni Kharadze Georgian National Astrophysical Observatory, Abastumani, 0301, Georgia

⁶Argelander-Institut für Astronomie, Universität Bonn, Germany

⁷Max-Planck-Institut für Radioastronomie, Bonn, Germany

March 3, 2022

ABSTRACT

The merger of two white dwarfs (WD) is a natural outcome from the evolution of many binary stars. Recently, a super-Chandrasekhar WD merger product, IRAS 00500+6713, was identified. IRAS 00500+6713 consists of a central star embedded in a circular nebula. The analysis of the optical spectrum of the central star revealed that it is hot, hydrogen and helium free, and drives an extremely fast wind with a record breaking speed. The nebula was first detected in infrared but it is not visible neither in the optical nor the UV. No nebula spectroscopy was obtained prior to our observations. Here we report the first deep X-ray imaging spectroscopic observations of IRAS 00500+6713. Both the central star and the nebula are detected in X-rays, heralding the WD merger products as a new distinct type of strong X-ray sources. Low-resolution X-ray spectra reveal large neon, magnesium, silicon, and sulfur enrichment of the central star and the nebula. We conclude that IRAS 00500+6713 resulted from a merger of an ONeMg and a CO WD, and that the merger was associated with an episode of carbon burning and possibly accompanied by a SN Iax. In X-rays, we observe the point source associated with the merger product while the surrounding diffuse nebula is a supernova remnant. IRAS 00500+6713 will likely terminate its evolution with another peculiar Type I supernova, where the final core collapse to a neutron star might be induced by electron captures, and possibly produce a millisecond pulsar.

Key words. white dwarfs – X-rays: stars – ISM: supernova remnants – Stars: evolution

1. Introduction

White dwarfs (WD) are the degenerate remnants of stars born with initial mass $M_{\text{init}} \lesssim 10 M_{\odot}$. WDs orbiting each other in a binary system emit gravitational waves leading to the gradual orbit shrinking and the eventual merger. The WD mergers are accompanied by explosive events, and the outcome of the merger depends on the chemical compositions and masses of involved WDs. Likely the most common outcome is a supernova (SN) type Ia which completely disrupts the merger product (Maoz et al. 2014). However, when a WD involved in a merger descends from an intermediate mass star ($M_{\text{init}} \approx 8 \dots 10 M_{\odot}$), the merger could eventually lead to a creation of a neutron star (NS, Saio & Nomoto 2004). Schwab et al. (2016) showed that a merger of two carbon-oxygen WDs can result in a stable, super-Chandrasekhar mass, object. A creation of a super-Chandrasekhar object could also result from a merger of even more massive WDs accompanied by a peculiar supernova, e.g. SN Iax (Bhattacharya & van den Heuvel 1991; Kashyap et al. 2018). However, while expected to be numerous, neither the remnants of such supernovae nor the surviving merger products have been firmly identified.

Recently, a super-Chandrasekhar mass object, IRAS 00500+6713, was detected by Gvaramadze et al. (2019). This object consists of a central star embedded in a circular nebula seen in mid-infrared (IR, Fig. 1). The analysis of the optical spectrum of the central star revealed that it is hot, hydrogen and helium free, consists mainly of carbon and oxygen, and drives a wind with a record breaking speed (Table 1). It was suggested that IRAS 00500+6713 resulted from the merger of two CO WDs, although a possibility was reserved that a higher mass ONe WD participated in the merger. Careful study of the available archival near-IR, optical, and UV observations did not reveal nebula emission at these wavelengths. Gvaramadze et al. (2019) explained this by hydrogen- and helium-free composition of the nebula, and by the very high temperature of the central star (Table 1) which leads to the triple ionization of oxygen and explains the lack of observed nebula lines in the optical. No spectra of the nebula could be obtained and its chemical composition was not known preventing firm conclusions on the nature of WDs involved in the merger process and the fate of the merger product.

In this Letter we report first deep X-ray observation of IRAS 00500+6713 and the first spectroscopic investigation of the nebula. In section 2 we describe the new X-ray data. An X-

[★] Based on the observations with the id numbers 0841640101, 0841640201 obtained with the ESA science mission *XMM-Newton*.

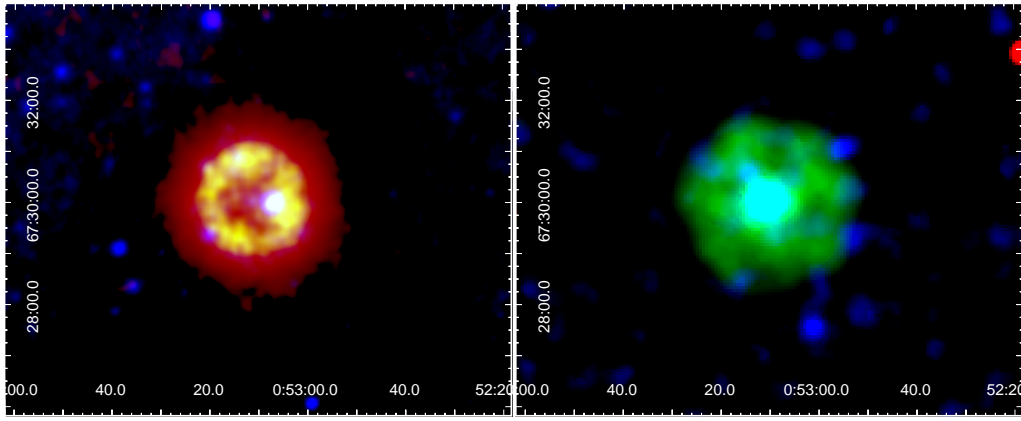


Fig. 1. Images of IRAS 00500+6713 in mid-IR and X-ray wavelength ranges. *Left panel:* IR *Wide-field Infrared Survey Explorer* (WISE) image: red and green correspond to $22\mu\text{m}$ at two intensity scales, blue corresponds to $12\mu\text{m}$. A ring-like structure with diameter $\sim 2'$ is seen within the nebula; *Right panel:* X-ray EPIC image: red: 0.2–0.7 keV, green: 0.7–1.2 keV, blue: 1.2–7.0 keV. The adaptively smoothed image shows that X-ray emission uniformly fills the whole $\sim 4'$ extent of the IR nebula. At the distance of IRAS 00500+6713, $1'$ corresponds to 0.86 pc. The coordinates are in units of RA (J2000) and Dec. (J2000) on the horizontal and vertical scales, respectively.

ray spectroscopic analysis of the central star is given in section 3, while the first nebula spectra are analyzed in section 4. Section 5 presents our explanations of the results and the concluding remarks, while detailed description of the X-ray fitting procedure is presented in the Appendix.

2. Observations: the central star and its nebula are luminous X-ray sources

Observations were obtained with the X-Ray Multi-Mirror Mission (*XMM-Newton*) of the European Space Agency (ESA). The three X-ray telescopes of *XMM-Newton* illuminate five different instruments, which always operate simultaneously and independently. The useful data were obtained with the three focal instruments: MOS1, MOS2 and PN, which together form the European Photon Imaging Camera (EPIC). The EPIC instruments have a broad wavelength coverage of $1.2 - 60\text{ \AA}$, and allow low-resolution spectroscopy with ($E/\Delta E \approx 20 - 50$). The log of the *XMM-Newton* observations is given in Table A.1. After rejecting high-background time intervals, the cumulative useful exposure time was $\approx 18\text{ ks}$ for the EPIC PN and $\approx 31\text{ ks}$ for the EPIC MOS cameras. The data were analysed using the *XMM-Newton* data analysis package SAS¹. Throughout this paper, X-ray fluxes and luminosities are given in the full 0.2–12.0 keV energy band, unless specified otherwise.

The *XMM-Newton* observations revealed astonishing X-ray properties of IRAS 00500+6713 (Fig. 1 and Table 1). Both the central star and the nebula are clearly detected, heralding the WD merger products as a new distinct type of strong X-ray sources. The X-ray luminosity of the central star falls in the upper range of luminosities known for accreting WDs in cataclysmic variables (Verbunt et al. 1997). However the H- and He-free chemical composition inferred from the analysis of the optical spectrum argues against accretion from a low-mass H-rich companion as expected for a cataclysmic variable. At the same time, the central star X-ray luminosity is significantly higher than in any other type of single star, including OB and Wolf-Rayet (WR) stars (Nebot Gómez-Morán & Oskina 2018). Similarly to the massive and more luminous H- and He-free WO stars, the optical spectrum of the central star in IRAS 00500+6713 is formed in its

powerful stellar wind. However, the X-ray luminosity of the latter is two orders of magnitude higher than X-ray luminosities of WO stars (Oskina et al. 2009).

3. Analysis of the central star X-ray spectra uncovers carbon and oxygen burning ashes

The X-ray spectra (Fig. 2) and the central star light curve (Fig. A.1) were extracted using standard X-ray analysis tools (see Appendix) from a circle with diameter $20''$. As the background area, we selected an annulus which traces the full extent of the diffuse X-ray emitting nebula around the point source. Hence, the contribution of the nebula emission to the spectrum of the central star should be small. The pile-up is negligible.

The PN light curve binned by 600 s is shown in Fig. A.1. The standard timing analysis procedures were employed to search for a period, but periodicity was not detected. In optical, photometric monitoring of IRAS 00500+6713 performed in 2017–2019 showed only small variability not exceeding 0.05 mag (Gvaramadze et al. 2019, A. S. Moskvitin, private communication).

The EPIC spectra were analysed using the spectral fitting software *xspecc* (Arnaud 1996). The spectra of collisionally-ionized optically thin plasma were computed with the *apex* model (and its modifications) and the corresponding atomic database *AtomDB* (Smith et al. 2001). The X-ray spectra are dominated by emission lines of Fe, as well as the products of He- and C-burning such as C, N, O, Mg, Ne, Si, and S (Fig. 2 and Fig. A.2). The metal abundances measured from the model fitting to the observed low-resolution spectra are shown in Table 1 using the procedure described in the Appendix C.

X-ray emitting plasma in the central star has a broad range of temperatures (Table 1 and Table A.2) – assuming purely thermal plasma, temperatures up to $\sim 100\text{ MK}$ are required to reproduce the observed spectra. On the other hand, including a non-thermal spectral component described by a power-law improves the spectral fits. In this case, the maximum thermal plasma temperature is $\sim 20\text{ MK}$. Plasma could be heated to such high temperatures by the shocks in the stellar wind of central star in IRAS 00500+6713, while the non-thermal radiation could be powered by particle acceleration in the expected presence of a magnetic field (Gvaramadze et al. 2019).

The central star in IRAS 00500+6713 has high a mass-loss rate and a CO-rich wind which should effectively absorb X-rays.

¹ www.cosmos.esa.int/web/xmm-newton/what-is-sas

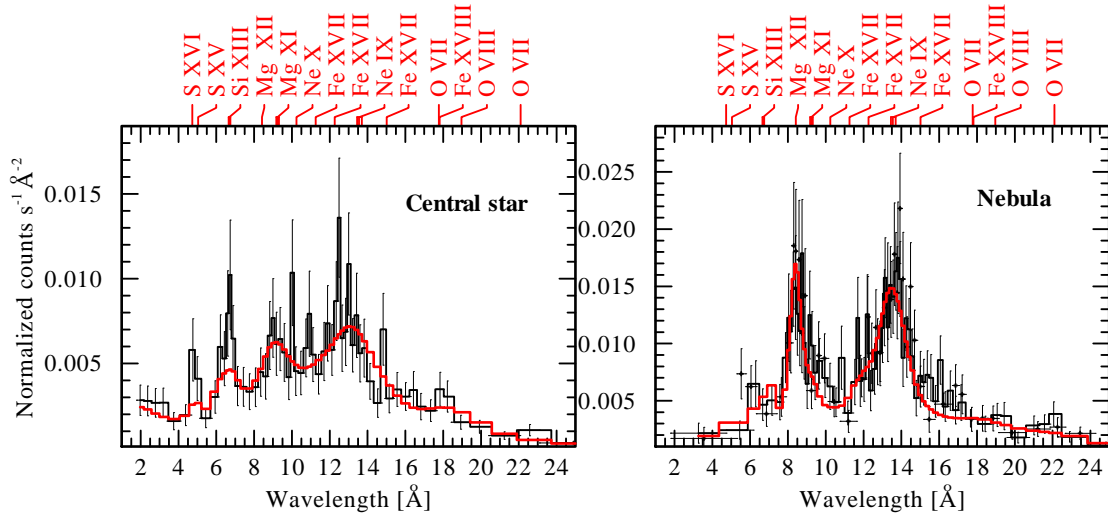


Fig. 2. Low resolution EPIC PN X-ray spectra of the central star (left panel) and the nebula (right panel) in IRAS 00500+6713. The error bars correspond to 3σ . Red histograms show the best-fitting spectral models (Table 1).

We searched for the presence of K-shell edges in the X-ray spectrum of the central star, but could not confidently detect them. This rules out an origin of X-ray emission at the base of the wind, or implies that the hot and cool wind components are spatially distinct.

The optical spectrum of the central star has WR-type and is dominated by strong emission lines of C and O. The optical spectrum was analyzed by means of a non-local thermodynamic equilibrium stellar atmosphere model (which did not account for X-rays). The carbon and oxygen abundances were derived and resulted in the ratio $(C/C_{\odot})/(O/O_{\odot}) \approx 0.6$ (by number) (Gvaradze et al. 2019). The optical spectrum analyses also hinted on strong Ne enrichment, up to 50% by mass, but magnesium, silicon, and sulfur were not included in the models. In X-ray spectra, the carbon lines are located redwards of 30 \AA , i.e. in the spectral range which suffers from the absorption of X-rays in the interstellar medium. Consequently, carbon lines are not detected in the central star X-ray spectra. Hence, during the analysis of X-ray spectra we adopted the carbon abundance as well as the C/O ratio as derived from optical spectroscopy.

The spectral models which well reproduce the observed X-ray spectra of the central star (Table A.2) have similar abundance ratios and require strong enhancement of carbon-burning ashes, as well as of Si and S. The emission features corresponding to the blends of Si XIII $\lambda 6.65 \text{ \AA}$ and Si XIV $\lambda 6.18 \text{ \AA}$ lines, as well as of S XV $\lambda 5.04 \text{ \AA}$ and S XVI $\lambda 4.73 \text{ \AA}$ lines are well seen in the spectra displayed in Fig. 2. These lines have their peaks at the temperatures between 10 MK and 26 MK, i.e. in the temperature range covered by our two-temperature spectral models. Therefore we believe that the strong Si and S overabundances detected in the X-ray spectra of the central star are real.

4. The lines of carbon burning ashes are detected in the nebula spectra

Here we present the first spectroscopy of the IRAS 00500+6713's nebula (Fig. 2). The nebula images and spectra were obtained with the help of the *ESAS* package which also computes the response functions for extended sources (Appendix B). The extent of the circular X-ray nebula is the same as of the IR nebula detected at $22 \text{ }\mu\text{m}$ (Fig. 1). Gvaradze et al. (2019) attributed the nebula emission to the forbidden lines

of [O IV] $\lambda 25.89 \text{ }\mu\text{m}$ and [Ne V] $\lambda\lambda 14.32, 24.32 \text{ }\mu\text{m}$. We suggest that the warm dust also contributes to the nebula IR emission. The warm dust co-existing with the hot plasma is often observed in the supernova remnants (SNR) (Zhou et al. 2020). The X-ray nebula is brightest in the medium X-ray band (0.7–1.2 keV). A number of faint X-ray point sources are superimposed on the nebula, for now we consider these sources as unrelated.

The X-ray luminosity of the nebula is in the upper range observed from hot bubbles around massive WR stars (Toalá et al. 2017), and significantly higher than the luminosity of diffuse gas in planetary nebulae (Chu et al. 2001; Kastner et al. 2001). Furthermore, the plasma temperature significantly exceeds the temperatures in WR bubbles or planetary nebulae. X-ray emission of these objects is powered by strong shocks which occur when the fast wind driven by the hot central stars rams into material of a slow wind ejected at previous stellar evolutionary stage. Hydrodynamic simulations of hot WR bubbles and planetary nebulae indicate that mixing processes effectively reduce possible differences in chemical composition of the cool and the hot gas components (Volk & Kwok 1985; Chevalier & Luo 1994; Kwok 2000; Toalá & Arthur 2011).

The IRAS 00500+6713 nebula spectrum is dominated by two strong emission features corresponding to the blends of the Mg XI $\lambda 9.1 \text{ \AA}$ and Mg XII $\lambda 8.4 \text{ \AA}$ lines and the Ne IX $\lambda 13.4 \text{ \AA}$ and Ne X $\lambda 12.1 \text{ \AA}$ lines (Figs. 2, A.3). The blend of the S XVI $\lambda 4.7 \text{ \AA}$ and S XV $\lambda 5 \text{ \AA}$ lines is dramatically weaker in the nebula spectrum compared to the spectrum of the central star. Significantly, the derived Mg and Ne abundances are much higher in the nebula than in the central star (Table 1 and Table B.1). The emission measure of the hot plasma in the nebula is $\sim 10^{55} \text{ cm}^{-3}$. Under the crude assumption of a uniform and constant density and the nebula composed solely from C, O, Ne and Mg, the total mass of hot gas is $\sim 0.1 M_{\odot}$ (see Appendix C).

5. IRAS 00500+6713: a post WD merger product embedded in a SN Iax remnant and evolving towards an electron capture SN

The high X-ray luminosities of the central star and nebula imply the occurrence of violent hydrodynamic or magneto-hydrodynamic interactions in these objects. Additionally, our

Table 1. Parameters of the central star and the nebula in IRAS 00500+6713 determined from optical (Gvaramadze et al. 2019) and X-ray (this work) spectroscopy. The distance 3.1 kpc is adopted.

Central star parameters from optical spectroscopy	
$E(B - V)$ [mag]	0.84 ± 0.04
T_* [kK]	211^{+40}_{-23}
$\log L_{\text{bol}}/L_{\odot}$	4.6 ± 0.14
$\log L_{\text{mech}} [\text{erg s}^{-1}]$	≈ 38.4
Mass-loss rate \dot{M} [$M_{\odot} \text{ yr}^{-1}$]	$(3.5 \pm 0.6) \times 10^{-6}$
Wind velocity v_{∞} [km s^{-1}]	$16\,000 \pm 1\,000$
X_{C}	0.2 ± 0.1
X_{O}	0.8 ± 0.1
X_{Ne}	0.01
Central star parameters from X-ray spectroscopy	
N_{H} [cm^{-2}]	$(1.0 \pm 0.2) \times 10^{22}$
L_{X} (0.2–12 keV) [erg s^{-1}]	$(1.2 \pm 0.2) \times 10^{33}$
$\log L_{\text{X}}/L_{\text{bol}}$	≈ -5
$\log L_{\text{X}}/L_{\text{mech}}$	≈ -5
T_{X} [MK]	1–100
X_{C}	0.15
X_{O}	0.61
X_{Ne}	0.10 ± 0.3
X_{Mg}	0.04 ± 0.02
X_{Si}	0.06 ± 0.04
X_{S}	0.04
Nebula parameters from analyses of X-ray spectroscopy	
N_{H} [cm^{-2}]	$(0.8 \pm 0.2) \times 10^{22}$
L_{X} (0.2–12 keV) [erg s^{-1}]	$(3 \pm 0.2) \times 10^{34}$
T_{X} [MK]	1–20
X_{C}	0.70 ± 0.46
X_{O}	0.08 ± 0.07
X_{Ne}	0.15 ± 0.11
X_{Mg}	0.07 ± 0.05

The oxygen and carbon abundances were fixed during the fitting of the central star X-ray spectra, while only carbon abundance was fixed when fitting the nebula spectrum (see Appendix). The error bars correspond to 1σ .

sensitive spectroscopic X-ray observations revealed the presence of highly processed matter in the central star as well as in its nebula. It is insightful to compare these results with recent calculations of WD mergers and their further evolution.

The abundance constraints for the central star from Table 1, in particular the predominance of silicon and sulfur imply a composition resulting from incomplete carbon and oxygen burning. Indeed, assuming that no major element remained undetected, silicon and sulfur make up $\sim 10\%$ of the surface composition of the central star in IRAS 00500+6713, while neon and magnesium constitute up to $\sim 14\%$ of its composition. It turns out that such a bizarre surface chemistry has actually been predicted in recent WD merger calculations.

Hydrodynamic models of mergers between an ONeMg WD and a CO WD show that the less massive but larger CO dwarf is tidally disrupted and forms a hot, low-density accretion disk around the ONeMg dwarf (Kashyap et al. 2018). The ignition and explosive disruption of this disk produces a low-energy ($\sim 10^{49}$ erg) supernova, putatively of Type Iax, which leaves the ONeMg WD largely intact. In these models, the remaining WD re-accretes part of the explosive ejecta, which is highly enriched in Si and S (Kashyap et al. 2018, their Figs. 5 and 6), together

with Ne, Mg and unprocessed C and O. The final mass of the star left behind in this model is $\sim 2.2 M_{\odot}$.

In this scenario, the IRAS 00500+6713 nebula is in fact a SNR. Scaling relations based on Sedov-Taylor solution for the expanding adiabatic blast-wave (Borkowski et al. 2001; Oskina 2005) yield the SNR age of $\sim 10^3$ yr. The supernova (SN) following the merging of the WDs could thus have been observed at that time. However, Type Iax SNe can be as dim as $M_v = -14$ mag. The supernova would then only appear as bright as Sirius ($m_v = -1.5$ mag), and with a duration of just 2 weeks it could have easily been missed.

The inner ring-like shell seen in the IR image (Fig. 1, left panel) could have been created by the current fast wind of the central star. In this case, the size of the inner shell is equal to the distance at which the wind ram pressure is balanced by the thermal pressure in the SNR:

$$R_0 = \left[\frac{\dot{M} v_{\infty}}{4\pi P_{\text{th}}} \right]^{1/2}, \quad (1)$$

where $P_{\text{th}} = (\gamma - 1)E_{\text{th}}/V$, $\gamma = 5/3$, E_{th} is the thermal energy of the SN blast wave, $V = (4\pi/3)R_{\text{SNR}}^3$, and R_{SNR} is the radius of the SNR (i.e. of the full extent of the nebula). In the Sedov phase about 72% of the kinetic energy produced by the supernova explosion, E_0 , is converted into E_{th} , i.e. $E_{\text{th}} = 0.72E_0$. Adopting $E_0 = 2.2 \times 10^{49}$ erg (Kashyap et al. 2018), $E_{\text{th}} = 1.58 \times 10^{49}$ erg. Using the mass-loss rate and the wind speed of the central star in IRAS 00500+6713, (\dot{M} and v_{∞} from Table 1), the full nebula radius of 1.6 pc, and the above value of E_{th} , one finds that $P_{\text{th}} = 2.1 \times 10^{-8}$ dyne cm^{-2} and $R_0 = 0.38$ pc. This is a factor of 3 smaller than the radius of the inner shell, $R_{\text{sh}} = 1.1$ pc. The agreement between R_0 and R_{sh} would be better if E_0 were an order of magnitude lower, perhaps indicating the merged WDs were less massive. However, recalling that the thermal pressure within a SNR is not a constant value, but grows with radius, the assumption on a small E_0 may be not required in more detailed computations.

The SNR scenario on the nature of the nebula in IRAS 00500+6713 implies that the merger event happened very recently. For $E_0 = 2.2 \times 10^{49}$ erg and $n_{\text{ISM}} = 1 \text{ cm}^{-3}$, the age of the SNR is only $t_{\text{SNR}} \approx 350$ yr, while for a factor of ten lower value of E_0 , the SNR age is $t_{\text{SNR}} \approx 1100$ yr. These should be the characteristic times for the merger product to contract to its current size and to develop its very fast wind.

Whether ignition of the disrupted CO WD develops a supernova may depend on the masses of the merging WDs. Earlier, lower mass hydrodynamic models of the merging of an ONe (1.2 M_{\odot}) and a CO (0.6 M_{\odot}) WD (Lorén-Aguilar et al. 2009) find a rather mild nuclear processing of material from the CO dwarf, with some neon and magnesium production, but not compatible with the high Si and S abundances in IRAS 00500+6713. While the remnant WD mass of 1.5 M_{\odot} fits well to the mass of IRAS 00500+6713 as estimated from its current luminosity, the absence of a mass-luminosity relation for this type of objects precludes a firm mass determination.

Clearly, more WD merger models are needed to pin down the progenitor masses of the two WDs which produced IRAS 00500+6713. However, its high heavy element abundances reinforce the conclusion that this star's mass exceeds the Chandrasekhar limit. Whereas current models of WD mergers do not include stellar winds, the discovery of an extreme WO-type wind from the central star in IRAS 00500+6713 demonstrates the urgent need to do so, at least in models of post WD-merger evolution. As the merger products are naturally close to their Ed-

dington limit, they are expected to launch similar WO-type stellar winds, as soon as they reach high enough surface temperatures during their post-merger evolution (Gräfener & Vink 2013; Sander et al. 2020). However, the outstandingly high wind speed of IRAS 00500+6713 can only be understood in the framework of rotating magnetic winds (Poe et al. 1989; Gvaramadze et al. 2019; Kashiya et al. 2019), which argues for strong magnetic fields being produced during the merger.

Based on its empirical mass loss rate and the expected short remaining life time of several 1000 yr, the mass of IRAS 00500+6713 will likely remain above the Chandrasekhar limit. Its fate will therefore be to undergo core collapse and to form a neutron star, perhaps even a millisecond pulsar, residing in an old stellar population. In the course of this event, IRAS 00500+6713 will manage to produce its second supernova, in the form of a fast blue optical transient (Dessart et al. 2006; Lyutikov & Toonen 2019).

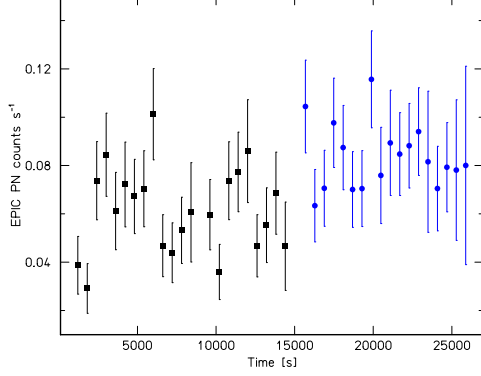
Acknowledgements. L.M.O. acknowledges financial support by the Deutsches Zentrum für Luft und Raumfahrt (DLR) grant FKZ 50 OR 1809, and partial support by the Russian Government Program of Competitive Growth of Kazan Federal University. V.V.G. acknowledges support from the Russian Science Foundation under grant 19-12-00383. G.G. thanks the Deutsch Forschungsgemeinschaft for financial support under Grant No. GR 1717/5-1.

References

- Arnaud, K. A. 1996, in *Astronomical Society of the Pacific Conference Series*, Vol. 101, *Astronomical Data Analysis Software and Systems V*, ed. G. H. Jacoby & J. Barnes, 17
- Asplund, M., Grevesse, N., Sauval, A. J., & Scott, P. 2009, *ARA&A*, 47, 481
- Bhattacharya, D. & van den Heuvel, E. P. J. 1991, *Phys. Rep.*, 203, 1
- Bohlin, R. C., Savage, B. D., & Drake, J. F. 1978, *ApJ*, 224, 132
- Borkowski, K. J., Lyerly, W. J., & Reynolds, S. P. 2001, *ApJ*, 548, 820
- Chevalier, R. A. & Luo, D. 1994, *ApJ*, 421, 225
- Chu, Y.-H., Guerrero, M. A., Gruendl, R. A., Williams, R. M., & Kaler, J. B. 2001, *ApJ*, 553, L69
- Dessart, L., Burrows, A., Ott, C. D., et al. 2006, *ApJ*, 644, 1063
- Gräfener, G. & Vink, J. S. 2013, *A&A*, 560, A6
- Gvaramadze, V. V., Gräfener, G., Langer, N., et al. 2019, *Nature*, 569, 684
- Kashiya, K., Fujisawa, K., & Shigeyama, T. 2019, *ApJ*, 887, 39
- Kashyap, R., Haque, T., Lorén-Aguilar, P., García-Berro, E., & Fisher, R. 2018, *ApJ*, 869, 140
- Kastner, J. H., Vrtillek, S. D., & Soker, N. 2001, *ApJ*, 550, L189
- Kwok, S. 2000, *The Origin and Evolution of Planetary Nebulae*
- Lorén-Aguilar, P., Isern, J., & García-Berro, E. 2009, *A&A*, 500, 1193
- Lyutikov, M. & Toonen, S. 2019, *MNRAS*, 487, 5618
- Maoz, D., Mannucci, F., & Nelemans, G. 2014, *ARA&A*, 52, 107
- Nebot Gómez-Morán, A. & Oskinova, L. M. 2018, *A&A*, 620, A89
- Oskinova, L. M. 2005, *MNRAS*, 361, 679
- Oskinova, L. M., Hamann, W. R., Feldmeier, A., Ignace, R., & Chu, Y. H. 2009, *ApJ*, 693, L44
- Poe, C. H., Friend, D. B., & Cassinelli, J. P. 1989, *ApJ*, 337, 888
- Saio, H. & Nomoto, K. 2004, *ApJ*, 615, 444
- Sander, A. A. C., Vink, J. S., & Hamann, W. R. 2020, *MNRAS*, 491, 4406
- Schwab, J., Quataert, E., & Kasen, D. 2016, *MNRAS*, 463, 3461
- Smith, R. K., Brickhouse, N. S., Liedahl, D. A., & Raymond, J. C. 2001, *ApJ*, 556, L91
- Snowden, S. L., Collier, M. R., & Kuntz, K. D. 2004, *ApJ*, 610, 1182
- Snowden, S. L., Mushotzky, R. F., Kuntz, K. D., & Davis, D. S. 2008, *A&A*, 478, 615
- Toalá, J. A. & Arthur, S. J. 2011, *ApJ*, 737, 100
- Toalá, J. A., Marston, A. P., Guerrero, M. A., Chu, Y. H., & Gruendl, R. A. 2017, *ApJ*, 846, 76
- Verbunt, F., Bunk, W. H., Ritter, H., & Pfeiffermann, E. 1997, *A&A*, 327, 602
- Volk, K. & Kwok, S. 1985, *A&A*, 153, 79
- Wilms, J., Allen, A., & McCray, R. 2000, *ApJ*, 542, 914
- Zhou, P., Leung, S.-C., Li, Z., et al. 2020, *arXiv e-prints*, arXiv:2006.15049

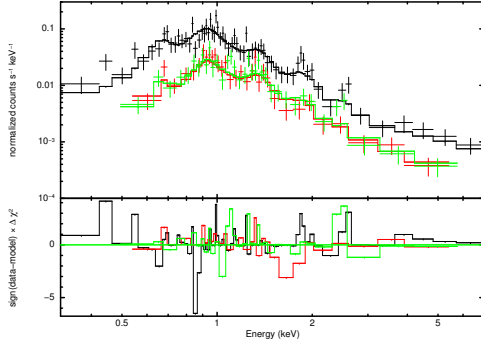
Table A.1. Log of the *XMM-Newton* observations of IRAS 00500+6713

ObsID	Start-date	exp. time [ks]
0841640101	2019-07-08	19.7
0841640201	2019-07-24	16.8

**Fig. A.1.** *XMM-Newton* EPIC PN light curve of the central star in IRAS 00500+6713. The light-curve is background corrected and is binned by 600 s, the error bars correspond to 3σ . The Y-axis is the time after the start of the observation. Black and blue data points refer to the first and second observation respectively (see Table A.1). For the second observation, the X-axis is shifted by 15 000 s for clarity.**Table A.2.** X-ray spectral properties of the central star in IRAS 00500+6713 from fitting its low-resolution EPIC spectra. The ion and the continuum temperatures are assumed to be equal. The line broadening is set to $v = 16000 \text{ km s}^{-1}$. The abundances shown without errors were not fitted but frozen during the fitting process. The abundances which are not shown in the table are at their solar values, except He and Ne which are vanishingly small. Observed flux and de-reddened luminosity are in 0.2-12.0 keV band assuming $d = 3.1 \text{ kpc}$.

Model parameter	fit value	
spectral model	<i>2Tbvtapec</i>	<i>2Tbvtapec+power</i>
N_H [10^{22} cm^{-2}]	1.0 ± 0.2	1.0 ± 0.2
kT_1 [keV]	0.27 ± 0.04	0.27 ± 0.04
EM_1 [10^{53} cm^{-3}]	2 ± 1	2 ± 1
kT_2 [keV]	6 ± 2	1.6 ± 1.1
EM_2 [10^{53} cm^{-3}]	0.8 ± 0.1	0.2 ± 0.1
C	600	600
O	1000	1000
Ne	800 ± 200	750 ± 200
Mg	600 ± 300	600 ± 250
Si	1000 ± 900	800 ± 520
S	1000	1000
α		0.9
K (ph $\text{keV}^{-1} \text{ cm}^{-2} \text{ s}^{-1}$)		$(4 \pm 1) \times 10^{-6}$
reduced χ^2	0.93	0.89
Model F_X [erg $\text{cm}^{-2} \text{ s}^{-1}$]	$1.7 \pm 0.2 \times 10^{-13}$	
Luminosity L_X [erg s^{-1}]	$(1.2 \pm 0.2) \times 10^{33}$	
$\log L_X/L_{\text{bol}}$	-5	

Appendix A: X-ray properties of the central star

**Fig. A.2.** Low-resolution X-ray spectra of the central star in IRAS 00500+6713. The EPIC PN (black data points), MOS1 (red data points) and MOS2 (green data points) spectra merged over the full exposure time are displayed. The black, red and green histograms show the best fitting model of a two-temperature plasma and a non-thermal components, and the residuals as signed contributions.

The spectra of the central star were extracted for each of the three EPIC cameras. The spectra obtained during each of the two observations (Table A.1) were combined using the *epic-speccombine* SAS task. The three resulting spectra are shown in Fig. A.2 were fitted using the *apec*, where the element abundances are normalized to solar values relative to hydrogen. Having this caveat in mind, the metal abundances measured from the model fitting to the observed low-resolution spectra shown in Tables A.2 and B.1 are relative to solar values Asplund et al. (2009).

Statistically acceptable fits to the observed spectra of the central star are obtained with the absorbed (by using the *tbabs* model

(Wilms et al. 2000)) multi-temperature *bvtapec*² spectral model. The stellar wind of IRAS 00500+6713 is exceptionally fast, with $v_\infty = 16000 \text{ km s}^{-1}$. If the hot plasma is expanding with similar velocity then emission lines observed in the X-ray spectrum are broad. The spectral resolution of EPIC cameras ($\Delta E = 20 - 50$) is not sufficient to resolve even such broad lines. Nevertheless, we found that accounting for line broadening (by setting the velocity parameter to 16000 km s^{-1}) improves the fitting statistics.

To determine the abundances, we first tested a model where the interstellar absorbing column density, N_H , and the C, O, N, Mg abundances were considered as free parameters; however no meaningful constraints on these parameters could be derived. The reddening to the star, $E(B - V)$, is known from the optical (Table 1). Hence, we tested a model with the fixed $N_H = 5.8 \times 10^{21} E(B - V)$ (Bohlin et al. 1978), however the metal abundances still could not be constrained. The C $\nu \lambda 41 \text{ \AA}$ and C $\nu \text{ Ly}\alpha \lambda 33 \text{ \AA}$ lines are located in the part of the *XMM-Newton* spectrum which has a low signal-to-noise ratio and which suffers from the absorption. Hence, X-ray spectral models are not sensitive to carbon abundances. Therefore, we decided to reduce the parameter space by using the abundance measurements from optical spectroscopy with the carbon and oxygen abundances determined as $C/C_\odot \approx 930$ and $O/O_\odot \approx 1500$ (by number, Gvarnadamze et al. 2019). Unfortunately, in *xspec* the maximum value of an element abundance is 1000. Therefore, we froze the O abundance to 1000 and set the C abundance to 600 to preserve the C/O ratio derived from the optical spectra.

A two temperature model with Ne, Mg, Si, and S abundances being fitting parameters tied among both temperature compo-

² A velocity- and thermally-broadened emission spectrum from collisionally-ionized diffuse gas calculated from the AtomDB atomic database, where we assumed identical “continuum” and “line” temperatures.

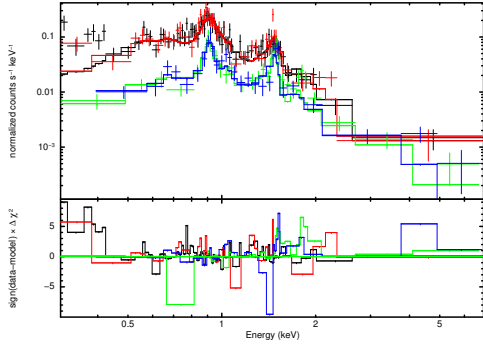


Fig. A.3. Low-resolution X-ray spectra of the nebula in IRAS 00500+6713. The EPIC PN (black and red data points) and MOS1 (blue and green data points) spectra obtained during two pointings are displayed. The histograms show the best-fitting model of a two-temperature plasma, and the residuals as signed contributions.

nents produces an excellent quality fit, indicating that S abundance is very high but very poorly constrained. The strong S line blend at $\lambda\lambda 4.7, 5.0 \text{ \AA}$ is well seen by eye. To roughly match the line strengths, we freeze the S abundance to the maximum possible value $S/S_{\odot}=1000$. This immediately improves the fitting statistics. The S xvi Ly α has the maximum emissivity at the temperature 25 MK. This temperature regime is covered by the hottest plasma component in our models, hence we believe that the large S abundance deduced from spectral fitting is real. The fitting statistics improve further when a non-thermal spectral energy component is included in the model (Table A.2 and Fig. A.2). Finally, the spectral models which include the K-shell edges were considered but no meaningful constraints on the presence of the edges could be obtained.

Appendix B: X-ray properties of the nebula

The Extended Source Analysis Software package (ESAS) Snowden et al. (2004, 2008) which is integrated in the SAS was employed to obtain the images and spectra of the diffuse emission. Following the data reductions steps prescribed by the *XMM-Newton* data analysis threads and the ESAS cookbook³, the EPIC images were created in “soft” (0.2–0.7 keV), “medium” (0.7–1.2 keV), and “hard” (1.2–7.0 keV) energy bands. The background was modelled and subtracted, and the individual images were merged after correcting them by their corresponding exposure maps. Each image in each band was adaptively smoothed requesting 50 counts under the smoothing kernel. The resultant exposure-corrected and background-subtracted colour-composite image of the sky in the vicinity of IRAS 00500+6713 is shown in Fig. 1.

The background and the point-source corrected spectra of the nebula, as well as the corresponding response matrices, were extracted for each camera (MOS1, MOS2, PN) and for each observation (Fig. A.3) using the *pn-spectra*, *pn-back*, and *mos-spectra*, *mos-back* tasks in the ESAS package. All spectra have been fitted simultaneously with the abundances tied between different model temperature components.

Two temperature plasma models well reproduce the spectra when abundances are allowed to vary. These are the first ever spectra of the nebula in IRAS 00500+6713, therefore there are no prior constraints on nebula abundances. From testing various models, the nitrogen abundance is not constrained and con-

Table B.1. X-ray spectral properties of the nebula in IRAS 00500+6713 from fitting its low-resolution EPIC spectra (see Fig. A.3). The spectral model is a combination of the *vapec* and the models corrected for the ISM absorption (*tbabs*). The abundances shown without errors were not fitted but frozen during the fitting process. The abundances which are not shown in the table are at their solar values. Observed flux and de-reddened luminosity are in 0.2–12.0 keV band assuming $d = 3.1 \text{ kpc}$.

Model parameter	fit value	
<i>xspec</i> spectral model	<i>tbabs(vapec+vapec)</i>	
$N_H [10^{22} \text{ cm}^{-2}]$	0.9 ± 0.1	0.8 ± 0.1
$kT_1 [\text{keV}]$	0.12 ± 0.01	0.13 ± 0.01
$EM_1 [10^{54} \text{ cm}^{-3}]$	16 ± 8	15 ± 8
$kT_2 [\text{keV}]$	1.7 ± 0.2	1.7 ± 0.2
$EM_2 [10^{54} \text{ cm}^{-3}]$	2.1 ± 0.3	1 ± 0.2
C	100	600
O	7 ± 4	30 ± 16
Ne	55 ± 17	240 ± 80
Mg	55 ± 12	210 ± 50
reduced χ^2	1.2	1.2
Model $F_X [\text{erg cm}^{-2} \text{ s}^{-1}]$	$(2.1 \pm 0.1) \times 10^{-13}$	
Luminosity $L_X [\text{erg s}^{-1}]$	$(3.0 \pm 0.2) \times 10^{34}$	

sistent with the absence of nitrogen. The absolute values of O, Ne, and Mg depend on the initial guess on the C abundance (Table B.1), however, importantly, independently on the assumed C-abundance, the relative to oxygen abundances are similar. Strikingly, these ratios are different from those derived for the central star (Table A.2).

Appendix C: Abundances

The abundances determined from the fitting of spectral models to the observed X-ray spectra of the central star and the nebula can be used to compute the metal mass ratios and fractions. We assume that all abundant elements are detected in optical and X-ray spectra. These elements are C, O, Ne, Mg, Si, and S. Denoting the mass fraction of *i*-element as X_i , and normalizing the total mass to unity gives $\sum_i X_i = 1$ or

$$X_i \sum_j \frac{X_j}{X_j} = 1 \quad (\text{C.1})$$

The element mass ratios are related to the element number fractions as

$$\frac{X_i}{X_j} = \frac{n_i}{n_j} \cdot \frac{A_i}{A_j}, \quad (\text{C.2})$$

where n_i is the abundance by number and A_i is the atomic mass of the element *i*.

The parameters of the X-ray spectral models *vapec* and *bv-tapec* which we use to fit the spectra with the *xspec* software are the metal element abundances by number relative to their solar values Asplund et al. (2009). Therefore,

$$\frac{X_i}{X_j} = \frac{n_i^{xspec}}{n_j^{xspec}} \cdot \frac{n_i^{\odot}}{n_j^{\odot}} \cdot \frac{A_i}{A_j}, \quad (\text{C.3})$$

then, using Eq. (C.1) and values given in Tables A.2 and B.1, one can derive the mass fractions X_i as given in Table 1.

From the analysis of the optical spectrum, $n_C = 0.25$ and $n_O = 0.74$, or $n_C/n_O = 0.3$. Using $n_i^{xspec} = n_i/n_C^{\odot}$, and calculating input parameters for carbon and oxygen, $n_C^{xspec} = n_C/n_C^{\odot} =$

³ <https://xmm-tools.cosmos.esa.int/external/sas/current/doc/esas/>

929.368, and $n_{\text{O}}^{\text{xspec}} = n_{\text{O}}/n_{\text{O}}^{\odot} = 1510.82$, hence as input ratio in *xspec* $n_{\text{C}}^{\text{xspec}}/n_{\text{O}}^{\text{xspec}} = 0.615$. Solving Eq. (C.1) gives $X_{\text{O}} = 0.6634$, and then $X_{\text{i}} = X_{\text{O}} \times \frac{X_{\text{i}}}{X_{\text{O}}}$.

To estimate the mass of hot gas in the nebula, we make a crude assumption that the nebula consists only of C, O, Ne, and Mg. Since X-ray emitting gas is hot, we assume that these ions are fully ionized. Assuming a constant density ρ , the spherical nebula mass is $M = \rho V = n_{\text{ion}} \mu m_{\text{H}} V$, where $V \approx 10^{56} \text{ cm}^3$. The emission measure of the nebula is $EM = V \mu \beta n_{\text{ion}}^2$, where $\beta \approx 1/2$ is the number of electrons per atomic mass unit, and $\mu = \sum A_{\text{i}} n_{\text{i}} / \sum n_{\text{i}} \approx 13$ is the mean ion mass. The EM is observationally constrained, inserting values from Table B.1 $M = m_{\text{H}} \sqrt{V \cdot EM \cdot \mu / \beta} \sim 0.1 M_{\odot}$.